



# A fixed mutation in the respiratory complex I impairs mitochondrial bioenergetics in the endangered Apennine brown bear

Emiliano Trucchi<sup>a,1,2</sup> , Silvia Fuselli<sup>b,1,2</sup> , Nunzio Perta<sup>a,c,d</sup> , Simone Patergnani<sup>e</sup>, Alberto Danese<sup>e</sup>, Dario Balestra<sup>b</sup> , Emidio Capriotti<sup>f</sup>, Giovanni Di Muccio<sup>a,c</sup>, Daniele Di Marino<sup>a,c,d</sup> , Paolo Pinton<sup>e</sup>, and Giorgio Bertorelle<sup>b,2</sup>

Affiliations are included on p. 9.

Edited by Ville R. Kaila, Stockholms Universitet, Stockholm, Sweden; received February 25, 2025; accepted August 7, 2025 by Editorial Board Member J. A. McCammon

Effective conservation genomics of endangered species requires realistic understanding of the fitness consequences caused by the accumulation of deleterious mutations in declining populations. We experimentally investigated three mutations which have been bioinformatically predicted to be deleterious in the mitochondrial ND5 subunit of respiratory complex I and are fixed in the Apennine brown bear, an inbred population of about 50 individuals isolated in Central Italy. Functional assays in transfected cell models and fibroblasts demonstrated that the G527E substitution significantly reduces mitochondrial transmembrane potential and calcium uptake by ca. 40 and 25% of the control level, respectively, while increasing reactive oxygen species production by ca. 45%. While further confirming these findings, experiments with bear fibroblasts highlighted lower oxygen consumption and impaired mitochondrial turnover in the Apennine bear. Molecular dynamics simulations uncovered structural effects of the G527E substitution, including increased rigidity of the ND5 and associated NDUF8 subunits and altered hydration dynamics in key aqueous channels of the complex I which are essential for proton pumping. These findings validate previous bioinformatic predictions of the negative fitness effects for one out of three mtDNA mutations, and elucidate the molecular mechanisms behind compromised bioenergetics in this endangered bear population produced by the G527E substitution. By linking genotype to phenotype via advanced molecular biology tools in a non-model species of conservation concern, this study highlights the need to fully integrate genomics and molecular experimental approaches in modern conservation biology.

deleterious mutation | respiratory complex I | molecular dynamics | conservation biology | bioenergetics

The accumulation in the genome of mutations with predicted deleterious effects (i.e., genetic load) can be used as a proxy for the reduction in Darwinian fitness of individuals and populations (1, 2), gaining momentum as a useful tool in conservation genomics (3–5). In non-model species, the fitness effect of a novel mutation is difficult to directly estimate and it is, instead, predicted using genome sequence annotation (e.g., refs. 6 and 7) or conservation scores across multispecies alignments (e.g., refs. 8 and 9). Mutations are predicted to be deleterious if they significantly alter the protein sequence or if they occur at nucleotide sites that have remained conserved across long evolutionary times. Novel approaches using deep learning algorithms to scan genetic sequence contexts have been recently proposed (10), holding promise to address some of the issues of existing tools.

Fitness predictions of novel mutations are hampered by several factors, including the inaccuracy of genome sequence annotations in several non-model species (11, 12), the limited statistical power in genomic regions that are difficult to align across species, and the difficulty to distinguish specific adaptations occurring only in one species (13). Whether bioinformatic predictions are accurate despite the complexity of the biological systems and the evolutionary history of a population or a species is therefore an open question. Advanced toolboxes in molecular biology and genetic engineering can address this question by enabling functional experiments (14, 15). This is specifically relevant to endangered species where the accumulation of genetic load can substantially increase the extinction risk and the choice of breeders for ex-situ or reintroduction plans should consider the genomic profile (4, 16).

A recent genomic study of the endangered Apennine bear population revealed 40 predicted deleterious mutations which are fixed in this small, isolated, and deeply inbred group

## Significance

Small populations can fix deleterious mutations through random genetic drift, providing opportunities to study such mutations in naturally evolving systems. By combining cellular experiments with molecular dynamics simulations, we demonstrate the functional consequences of a mutation (G527E in ND5) identified in the respiratory complex I of the endangered Apennine brown bear. This mutation substantially impairs complex I performance locally altering the flexibility and hydration dynamics of the inner water channels. Using an endangered bear population as a natural experiment, this study is of high interest to a broad scientific audience as it connects the fields of conservation genomics, experimental cell biology, and computational biophysics, providing insights relevant to fields far beyond wildlife conservation, including human mitochondrial diseases.

The authors declare no competing interest.

This article is a PNAS Direct Submission. V.R.K. is a guest editor invited by the Editorial Board.

Copyright © 2025 the Author(s). Published by PNAS. This article is distributed under [Creative Commons Attribution-NonCommercial-NoDerivatives License 4.0 \(CC BY-NC-ND\)](#).

<sup>1</sup>E.T. and S.F. contributed equally to this work.

<sup>2</sup>To whom correspondence may be addressed. Email: e.trucchi@univpm.it, silvia.fuselli@unife.it, or giorgio.bertorelle@unife.it.

This article contains supporting information online at <https://www.pnas.org/lookup/suppl/doi:10.1073/pnas.2504409122/-DCSupplemental>.

Published September 30, 2025.

of about 50 individuals distributed in a small area in Central Italy (17). According to the demographic reconstruction based on genomic data, the Apennine brown bear diverged from other European brown bear populations a few thousand years ago, suddenly declining to about one hundred individuals and maintaining such low population size since then. Strong genetic drift in this small population caused the complete loss of diversity in 75% of the genome (including the mitogenome), where long runs of homozygosity are interrupted by few high diversity regions which are enriched with olfactory receptors and immunity genes. The presence of such high diversity regions suggests that balancing selection could have still played a role despite the strong genetic drift or that molecular mechanisms like ectopic recombination helped retain diversity at highly duplicated genes. Three (P448S, G527E, and T556A) of the predicted deleterious mutations in the Apennine brown bear are in the mitochondrially encoded NADH-ubiquinone oxidoreductase chain 5 (17), a core subunit of the respiratory complex I, the largest of the mitochondrial electron transport chain enzymes responsible for proton translocation (Fig. 1). In humans, nuclear and mitochondrial mutations cause mitochondrial genetic disorders affecting multiple tissues or organs, especially those with high energy demand, such as the nervous system, heart, and skeletal muscles, as well as specific organs like the ear and the eye (18, 19). Causative mutations have been identified in mitochondrial genes encoding for all NADH dehydrogenase subunits in complex I. In particular, ND5 carries mutations associated with each of the best known mitochondrial diseases (20).

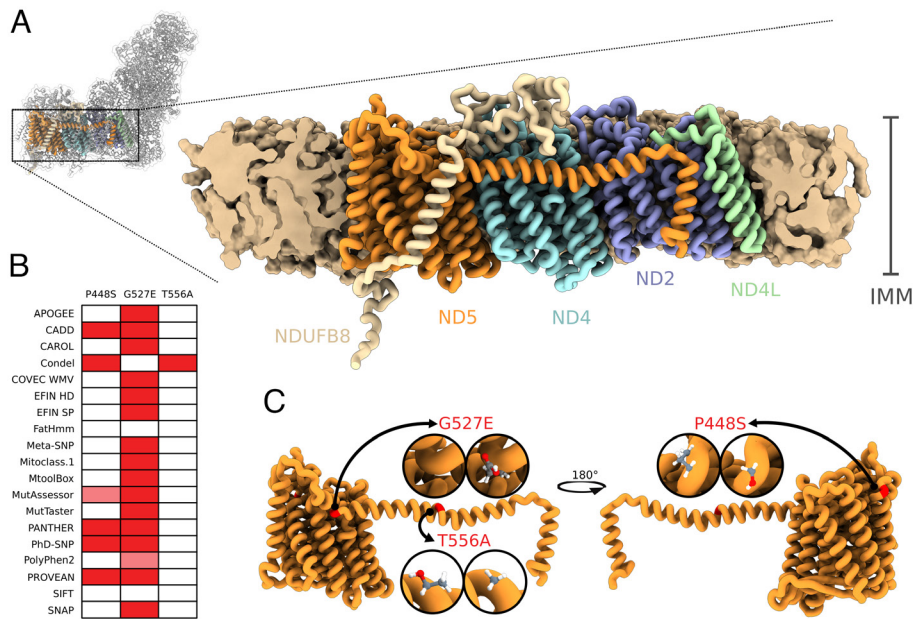
The ND5 deleterious mutations predicted in the Apennine bear are present in all sequenced mitogenomes in this inbred population (17), with a high potential for fitness impact (Fig. 1*B*): In particular, the G > E amino acid replacement at position 527 is unique to the Apennine bear when compared to other 5,000 carnivore sequences (BLAST search performed with default parameter,

database nt, organism: carnivores, January 2024), and it is classified (21, 22) as radical or extremely radical change, with a score of 0.86 on a range from 0 to 1 (23). The other two positions are more variable across carnivores and are classified as moderately conservative (P448S: 0.426; T556A: 0.486). Whether the predicted deleteriousness of the three ND5 mutations, and of the G527E in particular, translates into an actual functional impairment of ND5, or of the respiratory complex I as a whole, remains an open question. Addressing this question is crucial to determine whether commonly used predictions of mutation deleteriousness, based solely on genomic sequences, can be confidently used as proxies for fitness impairment. Specifically, estimating the real cellular effects of these mutations in the endangered and isolated Apennine bear population may be relevant for understanding their possible impact on survival and for guiding future protection strategies.

Here, we used Madin-Darby Canine Kidney (MDCK) cells transfected with edited (by site-directed mutagenesis) versions of ND5 and live bear fibroblasts with different mitochondrial haplotypes to show that the G527E functionally impairs mitochondrial bioenergetic performance, with higher ROS accumulation. Molecular dynamics simulations then highlighted a reduced flexibility in the portion of complex I near this mutation, along with an altered rate of water molecules movement through the aqueous channels which is crucial for complex I proton pumping.







Results

**Glutamic Acid in Position 527 of ND5 Compromises Mitochondrial Bioenergetics In Vitro.** MDCK cells were transfected with plasmids bearing five brown bear ND5 isoforms (see Table 1): one isoform bearing the three mutations together (i.e., *S448*, *E527*, *A556*; the *Apennine* bear haplotype), one for each of the three mutations separately, and one with the most common allele for each of these



**Fig. 1.** Apennine brown bear mutations in the ND5, one of the core subunits of the mitochondrial respiratory complex I. (A) Structure (PDB ID: 6ZR2) of the mitochondrial respiratory complex I (*Top Left*) and detailed view of the intermembrane (IMM) portion with the core chains ND5, ND4, and ND2, and ND4L, and the accessory chain NDUFB8, establishing contacts with ND5 (B) MitImpact 3D collection of genomic, clinical, and functional annotations for the three fixed substitutions (P448S, G527E, T556A) characterizing the Apennine bear mitochondrial ND5 in comparison with the major allele found across the whole European population (17). See <https://mitimpact.css-mendel.it/description> for references of the missense pathogenicity predictors and metapredictors (rows). Dark and light red indicates high and moderate predicted deleterious effects, respectively. (C) Positions on the ND5 structure and lateral amino acid residues of the three fixed substitutions present in the Apennine bear. Notably, the G527E mutation resides within the hinge region of ND5, situated at the beginning of the ND5 lateral helix that traverses the core central axis, interacting with all the aforementioned chains.

**Table 1. Different amino acid sequence versions of the ND5 at positions 448, 527, and 556 tested in this study**

Label	Color	ND5 positions			Experiments		
		448	527	556	MDCK cells	Fibroblasts	MD simulations
Apennine		S	E	A	X	X	X
S448		S	G	T	X		
E527		P	E	T	X		X
A556		P	G	A	X		
CTRL		P	G	T	X		X
Alpine		S	G	A		X	

We set up experiments with Madin-Darby Canine Kidney cells (MDCK), live brown bear fibroblasts, and molecular dynamics (MD) simulations. Labels and colors used in all figures are shown.

positions found in other European bear populations as a control (CTRL). All ND5 isoforms were successfully transported to and expressed in the MDCK mitochondria (SI Appendix, Fig. S1).

Both ND5 variants with the E527 resulted in markedly altered parameters of mitochondrial respiratory functions (Fig. 2). We observed a significant decrease in mitochondrial Calcium ( $\text{Ca}^{2+}$ ) uptake (Fig. 2A) and transmembrane potential ( $\Psi\text{m}$ ; Fig. 2B) by ca. 40 and 25% of the control level, respectively. On the other hand, we detected an increase in mitochondrial ROS production by ca. 45% as compared to the control (Fig. 2C). Cells transfected with the plasmids carrying the mutations in 448 and 556 showed no differences when compared to the control (Fig. 2).

**Mitochondrial Performance Is Lower in Apennine Bear Compared to Alpine Bear Cell Cultures.** The effect of the single amino acid replacement at position 527 of the ND5 was also analyzed in its native cell system, thus avoiding potential bias from protein overexpression. Mitochondrial functional parameters previously assessed in the MDCK cells were measured in primary fibroblast cells isolated from palatal biopsies (SI Appendix, Fig. S2). Two bears were analyzed: one from the Apennine population and the other from an Alpine population from Northern Italy. The latter was a descendant of a small group of Slovenian animals introduced during a translocation project in the 1990' (24). ND5 in the Alpine bear differs from that of the Apennine bear only at position 527 (ND5 - Apennine: S448, E527, A556; Alpine: S448, G527, A556, Table 1).

The Apennine bear fibroblasts show a 25 to 30% reduction in mitochondrial  $\text{Ca}^{2+}$  uptake and in  $\Psi\text{m}$  (Fig. 3 A and B), similar to that observed in the MDCK cell experiment. Furthermore, cells from Apennine bear were characterized by a marked increase in the production of mitochondrial ROS, more than double when compared to the Alpine bear (Fig. 3C). This outcome was also confirmed by measuring the oxygen consumption rate (OCR) of primary fibroblasts using the cell MitoStress test. Basal, ATP-related, and maximal respiration quantification calculated from OCR traces were significantly lower in Apennine vs. Alpine bear (Fig. 3E). These analyses provide further support for the effect of the glutamic acid in position 527 of the ND5 chain, deeply altering mitochondrial bioenergetic performance.

In addition, we observed a significantly lower respiratory complex I enzymatic activity in isolated mitochondria of the Apennine bear as compared to the Alpine bear (SI Appendix, Fig. S3A). We then assessed the protein levels of NDUFA5 (NADH:Ubiquinone Oxidoreductase Subunit A5), an essential and conserved accessory subunit of complex I involved in the transfer of electrons from NADH to ubiquinone. Western blot analysis did not reveal any

appreciable differences in NDUFA5 expression between the two bear populations, ruling out the possibility that the observed reduction in the Complex I activity was due to a decreased expression of the respiratory complex I (SI Appendix, Fig. S3B).

Finally, we tested whether the difference in OCR traces could be determined by the existence in the Apennine bear of a dysfunctional mitochondrial population with reduced turnover. If turnover works properly, the mitochondrial population undergoes coordinated renewal (mitobiogenesis) and degradation (mitophagy) processes, resulting in a healthy mitochondrial population (25). Using MitoTimer, a protein designed to track mitochondrial turnover labeling newly synthesized mitochondria in green and aged mitochondria in red (26), we found that the average age of mitochondria in the Apennine bear is older when compared to the Alpine bear (Fig. 3D).

**G527E Substitution Effects on Respiratory Complex I Internal Water Channels.** The molecular mechanism underlying the mitochondrial bioenergetic impairment caused by the G527E substitution was investigated through in silico molecular modeling—where initial folding of the core central-axis chains was predicted using AlphaFold2 (27)—and extensive all-atoms MD simulations carried out in GROMACS (28). In particular, we focused on a subset of chains within the core central axis of respiratory complex I (Fig. 1A), including the conserved core subunits ND5, ND4, ND2, and ND4L, as well as the supernumerary transmembrane helix NDUFB8 in close contact with ND5 (29). The molecular systems were completed via CHARMM-GUI membrane builder web server (30), embedding the modeled chains in a lipid bilayer (mimicking the inner mitochondrial membrane) and solvated into a 0.15 M NaCl water box, to form a minimal simulation module of approximately 640,000 atoms, as previously reported (31–34). We designed three distinct versions of the reduced respiratory complex I system to test the effect of glutamic acid in position 527: i) the Apennine bear haplotype, with all fixed mutations (16 in total, of which three in the ND5 including E527; Table 1) found in the core central axis of respiratory complex I; ii) a control haplotype with the most frequent European brown bear allele for all mutations found in the Apennine bear (including G527; CTRL); iii) a haplotype with the glutamic acid in 527 (E527) of the ND5 but the CTRL sequence for all other positions. For each system, we prepared three replicas and simulated each replica for 1.3  $\mu\text{s}$ , for a total of ~12  $\mu\text{s}$  MD sampling.

The simulations reveal that the G527E substitution has a significant impact on the structural stability of the ND5 and NDUFB8 subunits (Fig. 4), that are critical for stabilizing the



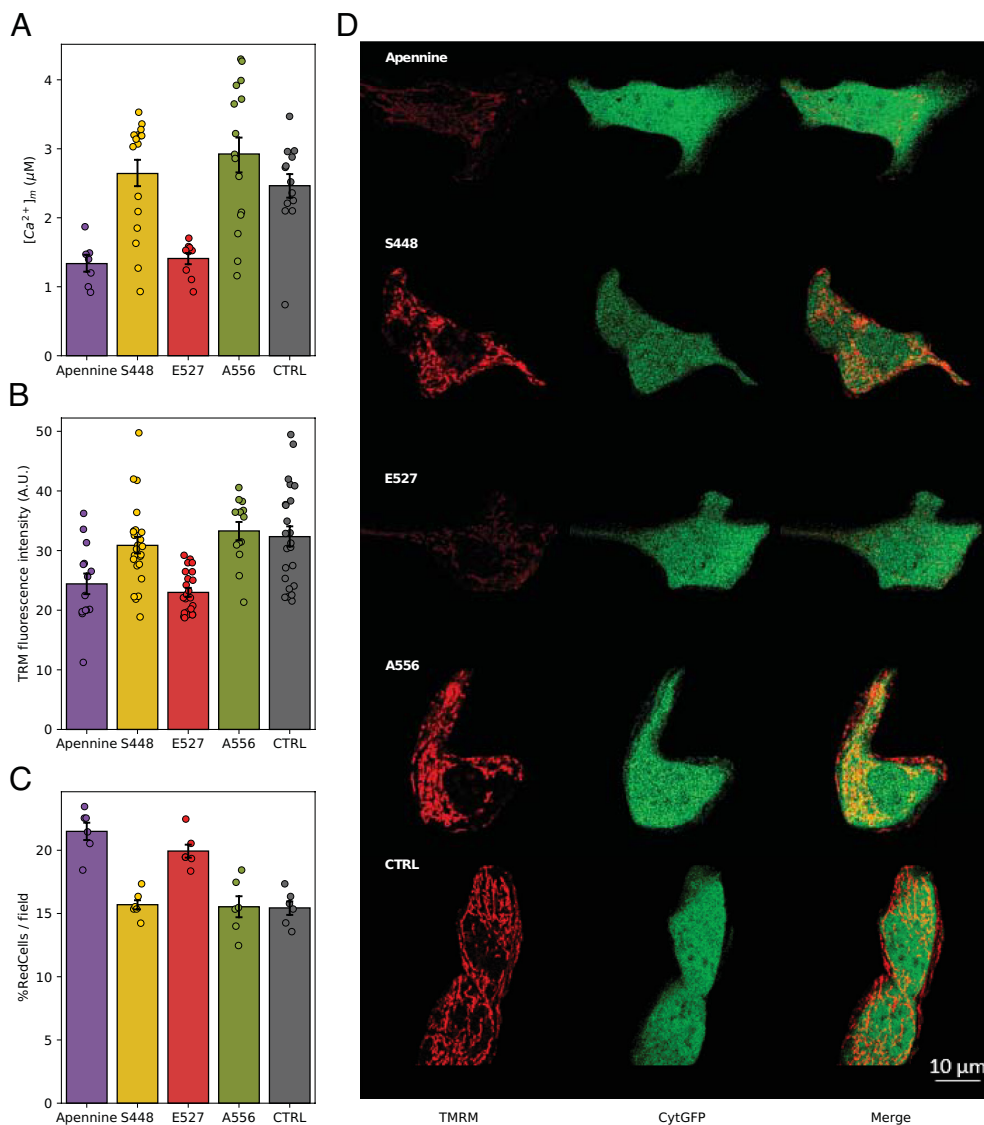


**Fig. 2.** Mitochondrial performance of different Apennine brown bear ND5 mutations in MDCK cells. (A) Mitochondrial  $Ca^{2+}$  response of cells cotransfected with mitochondrial-targeted aequorin and stimulated with 100  $\mu M$  ATP; ANOVA—Tukey's test significant differences: Apennine, E527 vs. CTRL ( $P$ -values < 0.01, both). (B) Transmembrane potential ( $\Psi_m$ ); ANOVA—Tukey's test significant differences: Apennine, E527 vs. CTRL ( $P$ -values < 0.01, < 0.0001, respectively). (C) Measurements of mitochondrial ROS production by using MitoSOX Red probe; ANOVA—Tukey's test significant differences: Apennine, E527 vs. CTRL ( $P$ -values < 0.0001, < 0.001, respectively). (D) Mitochondrial transmembrane potential ( $\Psi_m$ ) of MDCK cells overexpressing different ND5 subunits detected by the  $\Psi_m$ -sensitive probe TMRM (first column). After imaging,  $\Psi_m$  was depolarized by the mitochondrial uncoupler FCCP to exclude the nonspecific mitochondrial fluorescence. CytGFP was used to identify the mitochondrial-targeted ND5 constructs (second column). Replicates are indicated by circles in A–C, with bars and whiskers representing mean and SE.

entire complex (35, 36). This effect is primarily observed in two regions: i) the ND5 segment before position 527 (residues 483 to 519) and ii) the C-terminal region of NDUF8 (residues 43 to 117), both appearing as more rigid. At a closer inspection, the E527 substitution expands the network of interactions with neighboring residues within a 15 Å radius, leading to increased local rigidity compared to the original glycine residue (Fig. 4B). The projection of the MD trajectory along the first eigenvector of motion, obtained via the PCA analysis of the protein backbone atomic coordinates along the trajectory, confirms the overall increased stiffness of the ND5 chain when the glutamic acid is in position 527 (SI Appendix, Fig. S4 and Movie S1).

Next, we investigated whether the E527 substitution affects the water network inside the respiratory complex I. Thanks to their hydrophilic residues in the membrane domain, the water channels formed by the antiporter-like subunit ND5, ND4, and ND2, and ND4L are crucial for proton pumping (29, 32–34, 37, 38). First, we observed the spontaneous hydration of the aqueous channels

in the simulated versions of the respiratory complex I on a 1  $\mu s$  timescale (Fig. 4C and Movie S2) (see ref. 39). We measured the number of water molecules at equilibrium (i.e., 1,000 to 1,300 ns) in the whole aqueous system within the core central axis and within each of the aqueous channels separately (SI Appendix, Figs. S5 and S6), as described in (29). Across the different water channels, we observed the larger difference in average water content in the transversal channel connecting ND5 and ND4 (increase of 10 to 15% in both systems presenting the E527 mutation; Fig. 4D and SI Appendix, Fig. S6). This channel is highly conserved and crucial in connecting the central axis with the matrix (29).

## Discussion

**Bioinformatic Predictions and Real Effects.** The main motivation behind this study was to verify bioinformatic predictions regarding the damage caused by three mitochondrial mutations present in

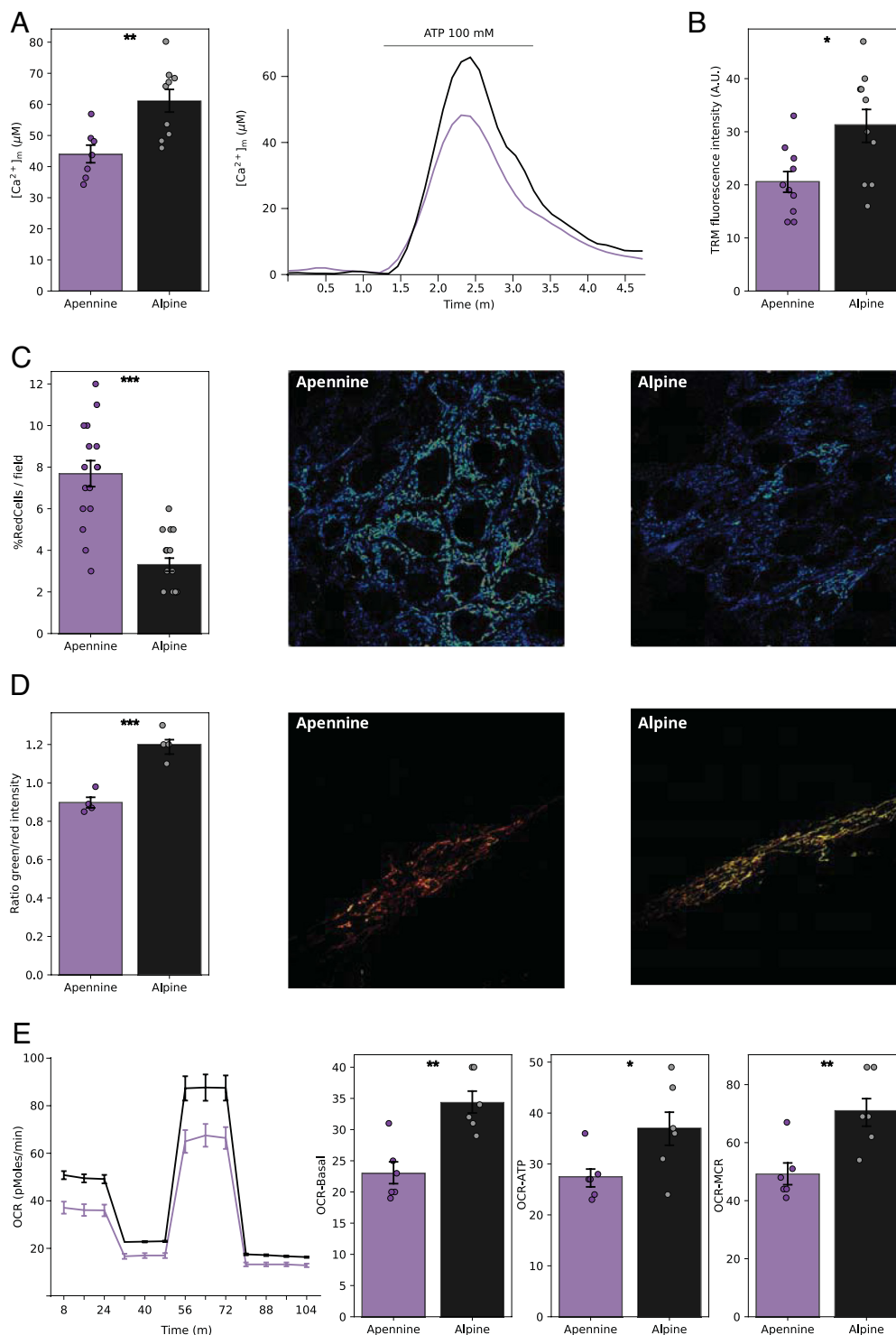


**Fig. 3.** Mitochondrial performance in fibroblasts sampled from Apennine and Alpine bears. (A) Mitochondrial  $Ca^{2+}$  response in replicated measurements (Left) and representative traces (Right) of fibroblasts infected with aequorin lentiviral vectors and stimulated with 100  $\mu M$  ATP. (B)  $\Psi_m$  assessment using the  $\Psi_m$ -sensitive probe TMRM. (C) Measurements of mitochondrial ROS production by using MitoSOX Red probe (Left); Apennine (center) and Alpine (Right) relevant images are shown. A LUT mask (Rainbow RGB) was applied to enhance the visualization of the probe signal intensity (D) Measurements of mitochondrial turnover using the fluorescent plasmid MitoTimer and shown as the ratio between green and red intensity, indicating young and old mitochondria (Left); Apennine (center) and Alpine (Right) relevant images are shown. (E) Normalized OCR traces (first panel) of Alpine and Apennine bear cell lines, expressed as pmol O<sub>2</sub>/min, in basal conditions and after the injection of oligomycin (1.5  $\mu M$ ; 24 min), FCCP (1  $\mu M$ , 48 min), ROT/AA (1  $\mu M$ , 72 min). Basal (second panel), ATP-related (third panel), and maximal (fourth panel) respiration (MRC) rates calculated from OCR traces. Replicates are indicated as circles with bars and whiskers representing mean and SE. Statistically significant difference between samples by the unpaired *t* test: \**P*-value < 0.05; \*\**P*-value < 0.01 \*\*\**P*-value < 0.001.

a crucial gene of the respiratory chain in the Apennine brown bears (17). Cellular experiments and molecular dynamics simulations performed in this study support the hypothesis of functional impairment and structural impacts of the G527E

mutation in the mitochondrial ND5 protein, suggesting potential clinical symptoms, still overlooked, which could exacerbate the conservation status of this small and endangered population. Often classified as a subspecies (*Ursus arctos marsicanus*), the

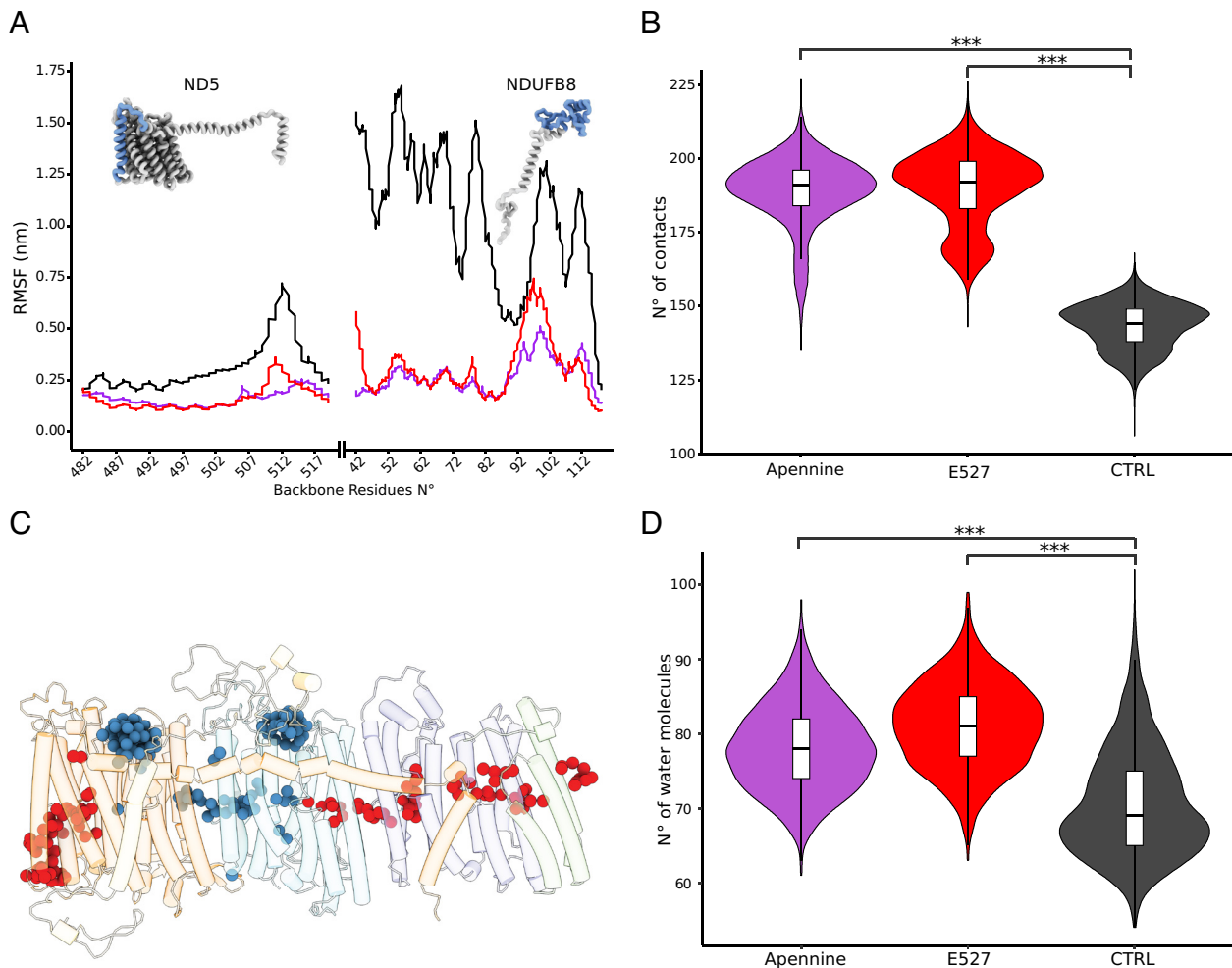


**Fig. 4.** Conformational and inner water channels dynamics of the respiratory complex I with the glycine or the glutamic acid in position 527 of the ND5. (A) Backbone RMS fluctuation (RMSF) profile for a portion of the ND5 (residues 483–519) and the NDUFB8 (residues 43–117) chain in Apennine (purple), E527 (red), and CTRL (black) molecular systems over simulation time. Portions of the subunits with the largest difference are shown in blue (B) Number of contacts between residue 527 of the ND5 chain and neighboring residues within 15 Å in the Apennine (purple), E527 (red), and the CTRL (black) molecular systems across three replicas per system over simulation time. (C) Inner water channel hydration at equilibrium after 1 μs simulation in the Apennine core complex I: Water molecules in the ND4-ND5 channel are shown as blue circles; water molecules in the rest of the channels are shown as red circles (see ref. 29) for channels identification and SI Appendix, Fig. S6A. (D) Hydration of the transversal ND5-ND4 inner water channel at equilibrium in the simulated Apennine, E527, and the CTRL core complex I. Differences between groups were analyzed by pairwise comparisons using the Wilcoxon test for independent samples with continuity correction; *P*-values were adjusted according to the Bonferroni method. \*\*\**P*-value < 0.001.

approximately 50 Apennine bears live in complete isolation from all other brown bear populations. The isolation can likely be attributed to habitat reduction and fragmentation related to the expansion of the agriculture practices in the Neolithic, and was accompanied by a severe bottleneck with consequent erosion of genomic variation (17). Genetic rescue is not recommended at the moment, considering that this population is genetically and phenotypically well differentiated from the geographic neighbors in Northern Italy and Slovenia, and recent simulations suggest that genetic load reduction would be transitory without a demographic increase (40). Understanding the real effects of fixed mutations, which were bioinformatically predicted to be deleterious, is relevant in general but crucial for this population. Bioinformatic predictions of deleteriousness have been frequently used in recent years to estimate the genetic load that could increase the risk of extinction in populations or species that have experienced recent bottlenecks due to anthropogenic factors (41–45). However, such predictions can be affected by errors (1, 2). Our functional and structural analyses confirmed these predictions for one mutation, while they were rejected for two others, which, however, had been predicted to have lower damage scores. This highlights the

importance of using predictive methods as tools for understanding the functional implications of genetic variation, while emphasizing the need to interpret results with caution, especially when predictions are based on intermediate scores.

**The Functional Impact of the G527E Mutation.** The transfection experiments in MDCK cells show that the G527E mutation can affect cellular metabolism and energy production. In fact, drops in  $\Psi_m$ , mitochondrial  $\text{Ca}^{2+}$  accumulation, and OCR are directly linked to a reduction in free energy, resulting in lower ATP production (25). The study on bears fibroblasts supports this view, and highlights the presence of a detrimental environment in Apennine bear mitochondria with an excess of ROS metabolites and a reduced mitochondrial turnover, which can compromise the overall cellular functions and dynamics (25). Importantly, the reduction in the respiratory complex I activity is not paired by a decreased expression (SI Appendix, Fig S3), providing further evidence to an actual malfunction of the protein system. The causative link between reduced mitochondrial performance as measured here, and lower cellular efficiency in energy production, is supported by several studies on human mitochondrial diseases.

For example, specific mutations of the mtDNA, causative for the LHON syndrome, provoke an increase in the oxidative stress, which, in turn, induces the loss of mitochondrial function and accelerates mitochondrial aging (46), leading to muscle weakness, fatigue, and ataxia. Also mutations in mitochondrial  $\text{Ca}^{2+}$  uniporter (a  $\text{Ca}^{2+}$  channel located in the inner mitochondrial membrane), which reduce  $\text{Ca}^{2+}$  uptake, cause atrophy of muscle cells and impair exercise performance, accelerating the onset of muscle fatigue (47).

**The Structural Impact of the G527E Mutation.** The molecular dynamics simulations suggest that the structural cause of the bioenergetic impairments associated with the G527E mutation is the increased rigidity in the ND5 and the NDUFB8 C-terminal regions. This rigidity results from an extended network of contacts involving the glutamic acid, which, in turn, appears to alter the hydration status of the ND5-ND4 hydrophilic channel—a crucial part of the internal water network responsible for proton pumping in the respiratory complex I. The G527E mutation lies at the hinge of the long transversal helix (TH) in the C-terminal part of ND5 which runs along the sides of subunits ND5, ND4, and ND2. It has been shown that a decreased stability of the TH portion could lead to a disconnection of the other antiporter-like subunits from the ND5-TH but without affecting proton pumping stoichiometry (48). In our mutated systems, on the contrary, we find an increased stability of the TH portion of the ND5 given by the substitution of a glycine with a charged glutamic acid. The increased stability may act as a constraint that prevents some antiporter-like movement by affecting the conformational changes of the functional residues of the proton translocation apparatus (32, 48, 49). This may then be responsible for the altered hydration at equilibrium observed in the Apennine bear transversal ND5-ND4 channel, which is essential for proton translocation (29), and, likely, for the reduced bioenergetic performance observed in the cellular experiments.

**Linking Structural and Functional Impacts of the G527E Mutation.** High-resolution structural analyses revealed extensive ordered water networks within the proton-conducting channels of complex I, where water molecules align to form continuous “water wires” critical for proton translocation (50, 51). These ordered waters interact intimately with conserved charged residues (e.g., Lys-Glu ion pairs) along channels, creating pathways that dynamically control proton movement (33, 50). Increased rigidity resulting from additional intraprotein contacts can directly impede necessary conformational rearrangements and disrupt internal water networks (33, 52). Even small alterations in hydration patterns can disrupt proton-conducting pathways, leading to impaired proton pumping and reduced mitochondrial membrane potential (53, 54).

Although an overall increase in hydration per se is less commonly highlighted than dehydration or disrupted hydration patterns, pathogenic mutations in ND5 and related subunits that alter the normal hydration network dynamics are known to significantly impair function. For instance, mutations such as ND5-F124L (Leigh syndrome) and ND4-R357H (LHON), while primarily reported to cause structural rigidity, simultaneously alter the positioning and interactions of internal water molecules (50, 52). Mutations such as V253A (MT-ND5) have also been shown to alter local contacts and disrupt critical hydrogen-bonding networks involving water molecules and gating residues, resulting in severe dysfunction (55). Increased, misplaced, or

disorderly waters around critical residues could similarly disrupt the precise hydrogen-bonding networks and negatively affect proton movement efficiency, analogous to how rigidity compromises necessary conformational flexibility (33, 54).

### Clinical Symptoms and Phenotypes in the Apennine Bear.

Given the impairment on mitochondrial performance caused by the G527E substitution, the small and isolated population of brown bears in Italy may exhibit clinical symptoms such as energy deficit, muscle weakness, and neurodegeneration. No detailed investigation has so far analyzed the presence of such phenotypes. A comparison with other brown bear populations on these traits is not available, though possible correlates have been identified: different skull morphology and smaller body size (56), higher levels of fluctuating asymmetry (57), predicted anomalies in cranial and skeletal development (17), and more docile behavior (genetically predicted and supported by absence of recorded attack to humans (17, 58). However, these traits can be found in other small and inbred mammal populations (59) and could be linked to other gene systems, not involving ND5 and the respiratory chain. On the other hand, it is also possible that yet undiscovered cellular or organismal mechanisms could be buffering the higher ROS accumulation and compensating the lower respiration efficiency observed in the Apennine bear. The drift to fixation of a deleterious mutation in a small population can occur when negative selection and dominance coefficients are not too large, when antagonistic pleiotropy is involved, and/or when ecological conditions change in a way that weakens purifying selection. At any rate, the absence of predators, the positive attitudes of the local communities toward bears (60, 61), and the availability of anthropic food, such as livestock, bees, and domestic fruits (62) could be the major factors allowing this population to thrive despite a fixed mitochondrial deficit. It is crucial to note that symptoms of mitochondrial dysfunctions are clinically variable, may manifest in childhood or only in adulthood, and are challenging to diagnose. Therefore, identifying such symptoms in animals remains a significant challenge. Enhanced and proactive monitoring of Apennine brown bear individuals, by assessing behavioral or physiological indicators of weakness or reduced energy production, could help identify the potential occurrence of these symptoms. This approach could also help determine whether individuals with different symptoms carry different variants in genes related to respiratory chain that could modify the penetrance of the G527E mutations.

### Conclusions

Novel approaches in conservation biology increasingly rely on genomic data (63). Here, we showed how advanced molecular biology techniques can also be applied to non-model species of conservation concern. Given the focus on the accumulation of deleterious mutations in endangered species and small populations (1, 2), going beyond the bioinformatic predictions provided by genomic studies is of the utmost importance. Molecular biology experiments can confirm or reject such predictions, provide enhanced power when selecting individuals for captive breeding or reintroduction programs by favoring those with reduced genetic load, and offer innovative biotechnological solutions (e.g., gene editing). At the same time, unraveling the molecular mechanisms behind natural conditions, such as those encountered in the Apennine brown bear mitochondria, may refine our understanding of fundamental cellular processes like the function of the respiratory complex I.



## Methods

**Mitochondrial-Targeted ND5 Constructs.** For the generation of mitochondrial-targeted ND5, we generated chimeric fusion proteins where a mitochondrial presequence (MTS) and the hemagglutinin (HA1) tag were added to the Apennine and non-Apennine ND5 proteins at the N and C termini, respectively. From the commonly reported MTS (from COX8A, COX10, and *S. cerevisiae* ATP3Δ), the MTS of COX8A was selected since having the highest mitochondrial score by using the DeepMito (<http://busca.biocomp.unibo.it/deepmito/>) tool (64). All proteins were codon-optimized for human expression and the coding cassettes were synthesized and sequence verified by Twist Bioscience (Twist Bioscience, San Francisco, CA) company. To evaluate the contribution of ND5 P448S, G527E, and T556A, all nucleotide substitutions were introduced into the Apennine bear sequence by using the Q5 Site-Directed Mutagenesis (New England Biolabs, Ipswich, MA) and the following primers: 5'-CCAGTTGG ATGGAGAATTTGAAAGGGTTC-3' and 5'-GATACTCCCATCATATCCACAGGC-3' for G527E, 5'-ACCTGGCTGGAAACGTGCTC-3' and 5'-TGATCCAACAGCATGTGGCC-3' for T556A, 5'-GGGGTTGTCTCATGATGATGATGACG-3' and 5'-CTGCTGATCAATCT ATTAAGCGGTG-3' for P448S. All mutants were verified by Sanger sequencing.

**Cell Culture and Transfection.** MDCK cells used in transfection experiments and bear fibroblasts were maintained in a humidified 5% CO<sub>2</sub> incubator at 37 °C in DMEM supplemented with 10% FBS (Life Technologies, 10270), 100 U/mL penicillin (EuroClone, 3001D), and 100 mg/mL streptomycin (EuroClone, 3000D). MDCK cells were transfected with a standard calcium phosphate procedure and with the polyethylenimine derivative jetPEI (Polyplus). For aequorin experiments, we used mitochondrial aequorin (mtAEQ). All measurements were performed 24 h after transfection.

**Measurement of Mitochondrial Parameters.** All mitochondrial parameters were measured in three to five different cell populations, replicated in cells plated in at least three different days. Mean values were statistically compared using *t* tests (when only two groups are compared) or ANOVA followed by Tukey's multiple comparisons test (when more than two groups are compared).

**Measurement of Aequorin to Estimate Ca<sup>2+</sup> Uptake.** Cells were grown on 13-mm round glass coverslips to 50% confluence and transfected with the appropriate mitochondrial (mt) targeted aequorin (Aeq). All aequorin measurements were performed in Krebs-Ringer buffer (KRB). Agonist (ATP, 100 μM) was added to the medium. The experiments were concluded by lysing the cells using 100 μM digitonin in a hypotonic solution containing 10 mM CaCl<sub>2</sub>, which facilitated the release of the remaining aequorin pool. The light emission was then captured and calibrated into calcium ion concentrations ([Ca<sup>2+</sup>]) based on previous methodologies (65).

**Measurement of ROS.** The total release of ROS from mitochondria was estimated fluorometrically by the oxidation of MitoSOX Red with a Tali™ image-based cytometer. The fluorescence levels of MitoSOX Red were measured at 510 ± 10 nm excitation and 595 ± 35 nm emission wavelengths (MitoSOX Red).

**Measurement of Ψ<sub>m</sub>.** The Ψ<sub>m</sub> was measured by labeling cells with 20 nM TMRM (Life Technologies: T-668) for 30 min at 37 °C. Images were taken on an inverted microscope (Nikon LiveScan Swept Field Confocal Microscope (SFC) Eclipse Ti equipped with Elements microscope imaging software). TMRM was excited at 560 nm, and the emission signal was collected through a 590 to 650-nm bandpass filter. Images were taken every 5 s with a fixed 20 ms exposure time. Carbonyl cyanide p-trifluoromethoxyphenylhydrazone (FCCP, 10 μM), an oxidative phosphorylation uncoupler, was added after 12 acquisitions to completely collapse the electrical gradient established by the respiratory chain.

**Measurement of OCR.** The rate of oxygen consumption was assayed with the XF96 Extracellular Flux Analyzer (Seahorse Biosciences–Agilent Technologies, Santa Clara, CA). Cells were plated 2 d before the experiment and allowed to reach a confluent monolayer. Briefly, mitochondrial respiration was evaluated by measuring the OCR under basal conditions and following the sequential addition of oligomycin (1 μM), carbonyl cyanide-4-(trifluoromethoxy)phenylhydrazone (FCCP, 2 μM), rotenone (1 μM), and antimycin A (1 μM). The different OCR parameters (basal respiration; maximal respiration; ATP production) were calculated as previously described (66). OCR values were normalized to the total

number of cells per well using the crystal violet staining method: Following the completion of the Seahorse assay, cells were fixed with paraformaldehyde (PFA) and stained with crystal violet. After thorough washing and drying, the bound dye was solubilized, and absorbance was measured at 595 nm. The absorbance values, which reflect the total cell number, were used to normalize the OCR data by entering them into the Seahorse software for automated normalization.

**Mitochondrial Isolation, Complex I Activity Assay and Immunoblot.** Intact mitochondria were isolated following the protocol published in (67). Briefly, cells were collected and homogenized in a specific isolation buffer and subjected to two centrifugation steps at 1,500×*g* for 5 min to remove nuclei and debris. The resulting supernatant was then centrifuged at 10,000×*g* for 10 min to pellet mitochondria. Pellets were resuspended in homogenization buffer (without digitonin) and centrifuged again at 10,000×*g* for 10 min for further purification. The final mitochondrial pellets were lysed in 100 μL of lysis buffer at 4 °C, incubated on ice for 30 min, and subsequently centrifuged at 17,000×*g* for 30 min. The resulting supernatants were collected, and protein concentration was determined using the Lowry method. Mitochondrial complex I activity was measured in isolated mitochondria by using the Mitochondrial Complex I Activity Colorimetric Assay Kit (Abcam, #ab287847), following the manufacturer's instructions. Absorbance was recorded at 600 nm in kinetic mode at 1-min interval. The enzymatic activity of mitochondrial complex I was calculated using the formula reported in the manufacturer's instructions:

Complex I Activity =  $\frac{\Delta[\text{reduced complex I dye concentration}]}{\Delta t \times p} \times D$ , where  $\Delta[\text{reduced complex I dye concentration}]$  = change in reduced dye concentration during the interval  $\Delta t$ ,  $\Delta t$  = time interval ( $t_2 - t_1$ , in minutes),  $p$  = amount of mitochondrial protein (μg),  $D$  = dilution factor.

Fifteen micrograms of isolated mitochondria were also subjected to immunoblotting to assess the levels of complex I subunits. Briefly, protein extracts were separated by SDS-PAGE using 4 to 12% precast gels (ThermoFisher, NW04125Box) and subsequently transferred onto nitrocellulose membranes. Membranes were then blocked for 1 h in TBS containing 0.05% Tween-20 and 5% nonfat dry milk to prevent nonspecific binding. Following blocking, membranes were incubated with the appropriate primary antibody overnight at 4 °C. After three washes, membranes were incubated with the corresponding HRP-conjugated secondary antibodies, exposed to a chemiluminescent substrate, and protein signals were detected using a GE ImageQuant imaging system. Antibody used: Anti-NDUFA5 antibody (Abcam, ab241492) and Anti-ATP5A (Abcam, ab176569). The latter was used as mitochondrial loading marker.

**MitoTimer Measurements.** Cells were transfected with the pTRE-tight-MITO TIMER plasmid (Addgene plasmid # 50547) (26). After 36 h, cells were imaged using excitation at 490 and 550 nm and emission of green (500 to 540 nm) and red (580 to 640 nm) fluorescence signals by using a Zeiss LSM510 confocal microscope and an Olympus scanning microscope equipped of 63x oil immersion objective (N.A. 1.4). The ratio of the fluorescence signal intensity in the red and green channels and the representative images were generated by using NIH ImageJ software as previously reported in (68).

**MD Simulations.** The 3D structures of the different versions of the respiratory complex I were constructed using their respective amino acid sequences (*SI Appendix, Table S2*) and the AlphaFold2 (AF2) predictor (27). Each complex included only a subset of chains: ND5, ND4, ND4L, ND2, and NDUFB8 (69). Three versions of the minimal transmembrane complex I were designed with different mutation on ND5: Apennine haplotype (S448, E527, A556), E527 (P448, E527, T556), and the CTRL haplotype (P448, G527, T556). For the E527, the glycine residue was replaced with glutamic acid on the ND5 structure by selecting the best-fitted sidechain rotamer from the Dunbrack library (70). To assemble the five-chain complex, each subunit obtained from the AF2 prediction was superimposed onto the cryoelectron microscopy structure of the respiratory complex I from *Mus musculus* in the active state (PDB ID: 6ZR2) (71) (*SI Appendix, Table S3*).

The systems were embedded in the inner mitochondrial membrane (IMM), the composition of which was adapted from CHARMM-GUI Archive (72) (*SI Appendix, Table S4*). All input files were generated using the CHARMM-GUI membrane builder web server (30). The process creates a rectangular simulation box, embedding the protein within the lipid bilayer and solvating the box using the TIP3P water model. The system charge was neutralized by introducing sodium and



chloride ions at 150 mM concentration. The MD simulations were performed using the GROMACS 2022.3 software using the CHARMM36m force field (28, 73).

Each system was subjected to 50,000 steps of minimization using the steepest descent algorithm. A simulated annealing protocol in the NVT ensemble was subsequently applied, with the temperature gradually and linearly increasing to the target temperature of 310.15 K over a period of 30 ns, using a time step of 1 fs. During this thermalization phase, positional restraints were imposed on the protein backbone ( $1,000 \text{ kJ mol}^{-1} \text{ nm}^{-2}$ ) and on side-chain atoms ( $100 \text{ kJ mol}^{-1} \text{ nm}^{-2}$ ). Then, after an NPT phase of 1 ns at 1 fs, eleven steps of 1 ns NVT were performed, each with a time step of 1 fs. In each NVT equilibration run, the positional restraints on the backbone and side-chain atoms were gradually reduced by  $100 \text{ kJ mol}^{-1} \text{ nm}^{-2}$  and  $10 \text{ kJ mol}^{-1} \text{ nm}^{-2}$ , respectively, until reaching  $0 \text{ kJ mol}^{-1} \text{ nm}^{-2}$ . The final NPT step was executed at a time step of 2 fs for 1 ns to prepare the system for the production run. The NPT equilibration utilized the C-rescale barostat (74) with a coupling time constant of 2 ps and a constant semi-isotropic pressure of 1 bar, in conjunction with the V-rescale thermostat with a coupling time constant of 2 ps (75). The production run employed the same barostat and thermostat settings as the last NPT run and lasted for a total of 1.3  $\mu\text{s}$ . The LINCS algorithm (76) was utilized to constrain the lengths of hydrogen bonds, while electrostatic interactions were computed through the particle mesh Ewald method (77), and a cutoff of 1.2 nm applied to the short-range nonbonded interactions. The same simulation protocol was applied for all the simulated systems. Two replicas were generated by reassigning the atomic velocities to 2 configurations taken at 5 ns (R1), and 15 ns (R2), from the production run respectively, in accordance with the required Maxwell-Boltzmann distribution. Each replica was carried out until a final time of 1.3  $\mu\text{s}$ .

We discarded from the structural analysis the first 0.5  $\mu\text{s}$  of the simulation runs that served as equilibration phase for the simulated systems as monitored by RMSD (Apennine  $0.41 \pm 0.06 \text{ nm}$ , E527  $0.47 \pm 0.09 \text{ nm}$ , and CTRL  $0.55 \pm 0.09 \text{ nm}$ , respectively, across replicates; *SI Appendix, Fig. S7*). RMSD, RMSF, the number of contacts, and motion PCA were carried out using tools within the GROMACS 2022.3 package (28). The motion projection along the first principal components was carried out using the "anaeig" tool within GROMACS, with a focus on the backbone atoms of protein chains, aiming to achieve a smoother depiction of the dynamics (78). Conserved residues used to calculate water

density in each inner channel were identified from key amino acids forming the water network in cryoelectron microscopy structure (PDB ID 80M1) (29). Water molecules calculations were conducted between 1  $\mu\text{s}$  to 1.3  $\mu\text{s}$ , following equilibration of the channels' hydration, which was monitored by calculating the number of waters within 6 Å of the central axis, as outlined by (37). For ND5 cavity, ND5-ND4, and ND4-ND2-ND4L channels (29), a 5 Å cutoff was applied. Figures and videos were generated using ChimeraX 1.7 molecular visualization program (79), and analyses were performed with VMD (80). All MD data are publicly available (81).

**Data, Materials, and Software Availability.** Molecular simulation data have been deposited in Zenodo (81). All other data are included in the manuscript and/or supporting information.

**ACKNOWLEDGMENTS.** This work was supported by the University of Ferrara (Italy) and funded by the Ministero dell'Università e della Ricerca (MUR) Progetti di Rilevante Interesse Nazionale (PRIN 2017 201794ZXTL) to G.B. S.P. was supported by the Italian Association for Cancer Research (AIRC, MFAG-29087), by Fondazione Italiana Sclerosi Multipla (FISM, 2022/RMulti/050, co-financed with the "5 per mille" public funding), by local funds of the University of Ferrara. P.P. was supported by local funds from the University of Ferrara, by Ministero dell'Università e della Ricerca (MUR, PRIN22 02259LHXM, PRIN22 PNRR P2022WY85K\_001), and by the Italian Association for Cancer Research (AIRC, IG-23670). A.D. is supported by Fondazione Umberto Veronesi.

Author affiliations: <sup>a</sup>Department of Life and Environmental Sciences, Marche Polytechnic University, Ancona 60131, Italy; <sup>b</sup>Department of Life Sciences and Biotechnology, University of Ferrara, Ferrara 44121, Italy; <sup>c</sup>New York-Marche Structural Biology Center, Department of Life and Environmental Sciences, Marche Polytechnic University, Ancona 60131, Italy; <sup>d</sup>Neuronal Death and Neuroprotection Unit, Department of Neuroscience, Mario Negri Institute for Pharmacological Research - Scientific Institute for Research, Hospitalization and Healthcare, Milano 20156, Italy; <sup>e</sup>Department of Medical Sciences, Laboratory for Technologies of Advanced Therapies, University of Ferrara, Ferrara 44121, Italy; and <sup>f</sup>Department of Pharmacy and Biotechnology, University of Bologna, Bologna 40126, Italy

Author contributions: E.T., S.F., and G.B. designed research; E.T., S.F., N.P., S.P., A.D., D.B., D.D.M., P.P., and G.B. performed research; N.P., S.P., A.D., D.B., E.C., G.D.M., and D.D.M. analyzed data; and E.T., S.F., N.P., and G.B. wrote the paper.

1. G. Bertorelle *et al.*, Genetic load: Genomic estimates and applications in non-model animals. *Nat. Rev. Genet.* **23**, 492–503 (2022).
2. N. Dussex, H. E. Morales, C. Grossen, L. Dalén, C. Oosterhout, Purging and accumulation of genetic load in conservation. *Trends Ecol. Evol.* **38**, 961–969 (2023).
3. J. Robinson, C. C. Kyriazis, S. C. Yuan, K. E. Lohmueller, Deleterious variation in natural populations and implications for conservation genetics. *Annu. Rev. Anim. Biosci.* **11**, 93–114 (2023).
4. C. Van Oosterhout, Mutation load is the spectre of species conservation. *Nat. Ecol. Evol.* **4**, 1004–1006 (2020).
5. A. P. Wilder *et al.*, The contribution of historical processes to contemporary extinction risk in placental mammals. *Science* **380**, 5856 (2023).
6. P. Cingolani *et al.*, A program for annotating and predicting the effects of single nucleotide polymorphisms, SnpEff: SNPs in the genome of *Drosophila melanogaster* strain w1118; iso-2; iso-3. *Fly* **6**, 80–92 (2012).
7. M. Kircher *et al.*, A general framework for estimating the relative pathogenicity of human genetic variants. *Nat. Genet.* **46**, 310–315 (2014).
8. E. V. Davydov *et al.*, Identifying a high fraction of the human genome to be under selective constraint using GERP++. *PLoS Comput. Biol.* **6**, 1001025 (2010).
9. K. S. Pollard, M. J. Hubisz, K. R. Rosenbloom, A. Siepel, Detection of nonneutral substitution rates on mammalian phylogenies. *Genome Res.* **20**, 110–121 (2010).
10. Y. Bromberg, R. Prabakaran, A. Kabir, A. Shehu, Variant effect prediction in the age of machine learning. *Cold Spring Harbor Perspectives in Biology* **16**, 041467 (2024).
11. G. F. Ejigu, J. Jung, Review on the computational genome annotation of sequences obtained by next-generation sequencing. *Biology* **9**, 295 (2020).
12. A. H. Freedman, T. B. Sackton, Building better genome annotations across the tree of life. *Genome Res.* **35**, 1261–1276 (2025).
13. C. D. Huber, B. Y. Kim, K. E. Lohmueller, Population genetic models of GERP scores suggest pervasive turnover of constrained sites across mammalian evolution. *PLoS Genet.* **16**, 1008827 (2020).
14. S. Mohammadi *et al.*, Epistatic effects between amino acid insertions and substitutions mediate toxin resistance of vertebrate Na<sup>+</sup>, K<sup>+</sup>-ATPases. *Mol. Biol. Evol.* **39**, msac258 (2022).
15. C. Sommer-Trembo *et al.*, The genetics of niche-specific behavioral tendencies in an adaptive radiation of cichlid fishes. *Science* **384**, 470–475 (2024).
16. E. J. Martin, S. A. Speak, L. Urban, H. E. Morales, C. Oosterhout, Sonification of genomic data to represent genetic load in zoo populations. *Zoo Biol.* **43**, 513–519 (2024).
17. A. Benazzo *et al.*, Survival and divergence in a small group: The extraordinary genomic history of the endangered Apennine brown bear stragglers. *Proc. Natl. Acad. Sci. U.S.A.* **114**, 9589–9597 (2017).
18. G. S. Gorman *et al.*, Mitochondrial diseases. *Nat. Rev. Dis. Primers* **2**, 1–22 (2016).
19. O. Rackham, A. Filipovska, Organization and expression of the mammalian mitochondrial genome. *Nat. Rev. Genet.* **23**, 606–623 (2022).
20. K. Fiedorczuk, L. A. Sazanov, Mammalian mitochondrial complex I structure and disease-causing mutations. *Trends Cell Biol.* **28**, 835–867 (2018).
21. S. Castellana, J. Rónai, T. Mazza, MitImpact: An exhaustive collection of pre-computed pathogenicity predictions of human mitochondrial non-synonymous variants. *Hum. Mutat.* **36**, 2413–2422 (2015).
22. S. Castellana *et al.*, MitImpact 3: Modeling the residue interaction network of the respiratory chain subunits. *Nucleic Acids Res.* **49**, 1282–1288 (2021).
23. J. Sharbrough, M. Luse, J. L. Boore, J. M. Logsdon, M. Neiman, Radical amino acid mutations persist longer in the absence of sex. *Evolution* **72**, 808–824 (2018).
24. G. Tosi *et al.*, Brown bear reintroduction in the Southern Alps: To what extent are expectations being met? *J. Nat. Conserv.* **26**, 9–19 (2015).
25. A. Suomalainen, J. Nunnari, Mitochondria at the crossroads of health and disease. *Cell* **187**, 2601–2627 (2024).
26. G. Hernandez *et al.*, MitoTimer: A novel tool for monitoring mitochondrial turnover. *Autophagy* **9**, 1852–1861 (2013).
27. J. Jumper *et al.*, Highly accurate protein structure prediction with AlphaFold. *Nature* **596**, 583–589 (2021).
28. M. J. Abraham *et al.*, GROMACS: High performance molecular simulations through multi-level parallelism from laptops to supercomputers. *SoftwareX* **1–2**, 19–25 (2015).
29. D. N. Grba, I. Chung, H. R. Bridges, A.-N. Agip, J. Hirst, Investigation of hydrated channels and proton pathways in a high-resolution cryo-EM structure of mammalian complex I. *Sci. Adv.* **9**, 1359 (2023).
30. E. L. Wu *et al.*, CHARMM-GUI membrane builder toward realistic biological membrane simulations. *J. Comput. Chem.* **35**, 1997–2004 (2014).
31. A. Beghiah *et al.*, Dissected antiporter modules establish minimal proton-conduction elements of the respiratory complex I. *Nat. Commun.* **15**, 9098 (2024).
32. A. Di Luca, A. P. Gamiz-Hernandez, V. R. I. Kaila, Symmetry-related proton transfer pathways in respiratory complex I. *Proc. Natl. Acad. Sci. U.S.A.* **114**, 6314–6321 (2017).
33. M. E. Mühlbauer *et al.*, Water-gated proton transfer dynamics in respiratory complex I. *J. Am. Chem. Soc.* **142**, 13718–13728 (2020).
34. M. Röpke *et al.*, Deactivation blocks proton pathways in the mitochondrial complex I. *Proc. Natl. Acad. Sci. U.S.A.* **118**, 2019498118 (2021).
35. A. Padavannil, M. G. Ayala-Hernandez, E. A. Castellanos-Silva, J. A. Letts, The mysterious multitude: Structural perspective on the accessory subunits of respiratory complex I. *Front. Mol. Biosci.* **8**, 798353 (2021).
36. D. Piekutowska-Abramczuk *et al.*, NDUF8 mutations cause mitochondrial complex I deficiency in individuals with leigh-like encephalomyopathy. *Am. J. Hum. Genet.* **102**, 460–467 (2018).
37. D. Kampjut, L. A. Sazanov, The coupling mechanism of mammalian respiratory complex I. *Science* **370**, 4209 (2020).

38. H. Kim, P. Saura, M. C. Pöörlein, A. P. Gamiz-Hernandez, V. R. I. Kaila, Quinone catalysis modulates proton transfer reactions in the membrane domain of respiratory complex I. *J. Am. Chem. Soc.* **145**, 17075–17086 (2023).
39. O. Zdorevskyi, A. Djurabekova, J. Lasham, V. Sharma, Horizontal proton transfer across the antiporter-like subunits in mitochondrial respiratory complex I. *Chem. Sci.* **14**, 6309–6318 (2023).
40. F. Maroso *et al.*, Fitness consequences and ancestry loss in the Apennine brown bear after a simulated genetic rescue intervention. *Conserv. Biol.* **37**, 14133 (2023).
41. N. Dussex *et al.*, Population genomics of the critically endangered kākāpō. *Cell Genom.* **1**, 100002 (2021).
42. J. I. Hoffman *et al.*, Genomic and fitness consequences of a near-extinction event in the northern elephant seal. *Nat. Ecol. Evol.* **8**, 2309–2324 (2024).
43. A. Khan *et al.*, Genomic evidence for inbreeding depression and purging of deleterious genetic variation in Indian tigers. *Proc. Natl. Acad. Sci. U.S.A.* **118**, 2023018118 (2021).
44. J. A. Robinson *et al.*, The critically endangered vaquita is not doomed to extinction by inbreeding depression. *Science* **376**, 635–639 (2022).
45. Q. Rougemont, T. Leroy, E. B. Rondeau, B. Koop, L. Bernatchez, Allele surfing causes maladaptation in a Pacific salmon of conservation concern. *PLoS Genet.* **19**, 1010918 (2023).
46. A. Danese *et al.*, Pathological mitophagy disrupts mitochondrial homeostasis in Leber's hereditary optic neuropathy. *Cell Rep.* **40**, 111124 (2022).
47. J. Q. Kwong *et al.*, The mitochondrial calcium uniporter underlies metabolic fuel preference in skeletal muscle. *JCI Insight* **3**, e121689 (2018).
48. O. D. Jarman, J. Hirst, Membrane-domain mutations in respiratory complex I impede catalysis but do not uncouple proton pumping from ubiquinone reduction. *PNAS Nexus* **1**, 276 (2022).
49. S. Zhu, S. B. Vik, Constraining the lateral helix of respiratory complex I by cross-linking does not impair enzyme activity or proton translocation. *J. Biol. Chem.* **290**, 20761–20773 (2015).
50. D. N. Grba, J. Hirst, Mitochondrial complex I structure reveals ordered water molecules for catalysis and proton translocation. *Nat. Struct. Mol. Biol.* **27**, 892–900 (2020).
51. K. Parey *et al.*, High-resolution structure and dynamics of mitochondrial complex I—insights into the proton pumping mechanism. *Sci. Adv.* **7**, 3221 (2021).
52. F. Hoerster, P. Saura, C. Harter, V. R. I. Kaila, T. Friedrich, A Leigh syndrome mutation perturbs long-range energy coupling in respiratory complex I. *Chem. Sci.* **16**, 7374–7386 (2025).
53. O. Haapanen, V. Sharma, Role of water and protein dynamics in proton pumping by respiratory complex I. *Sci. Rep.* **7**, 7747 (2017).
54. M. Röpke, P. Saura, D. Riepl, M. C. Pöörlein, V. R. I. Kaila, Functional water wires catalyze long-range proton pumping in the mammalian respiratory complex I. *J. Am. Chem. Soc.* **142**, 21758–21766 (2020).
55. F. Nuber *et al.*, Biochemical consequences of two clinically relevant ND-gene mutations in *Escherichia coli* respiratory complex I. *Sci. Rep.* **11**, 12641 (2021).
56. P. Colangelo *et al.*, Cranial distinctiveness in the Apennine brown bear: Genetic drift effect or ecophenotypic adaptation? *Biol. J. Linn. Soc.* **107**, 15–26 (2012).
57. A. Loy, P. Ciucci, G. Guidarelli, E. Roccatelli, P. Colangelo, Developmental instability and phenotypic evolution in a small and isolated bear population. *Biology Letters* **17**, 20200729 (2021).
58. G. Bombieri *et al.*, Brown bear attacks on humans: A worldwide perspective. *Sci. Rep.* **9**, 8573 (2019).
59. P. Crnokrak, D. A. Roff, Inbreeding depression in the wild. *Heredity* **83**, 260–270 (1999).
60. J. A. Glikman, B. Frank, D. D'Amico, L. Boitani, P. Ciucci, Sharing land with bears: Insights toward effective coexistence. *J. Nat. Conserv.* **74**, 126421 (2023).
61. P. Mayer, A. Grêt-Regamey, P. Ciucci, N. Salliou, A. Strith, Mapping human- and bear-centered perspectives on coexistence using a participatory bayesian framework. *J. Nat. Conserv.* **73**, 126387 (2023).
62. A. Donatelli, G. Mastrantonio, P. Ciucci, Circadian activity of small brown bear populations living in human-dominated landscapes. *Sci. Rep.* **12**, 15804 (2022).
63. K. Theissinger *et al.*, How genomics can help biodiversity conservation. *Trends Genet.* **39**, 545–559 (2023).
64. C. Savojardo, N. Bruciferri, G. Tartari, P. L. Martelli, R. Casadio, DeepMito: Accurate prediction of protein sub-mitochondrial localization using convolutional neural networks. *Bioinformatics* **36**, 56–64 (2020).
65. S. Patergnani *et al.*, PRKCB/protein kinase C, beta and the mitochondrial axis as key regulators of autophagy. *Autophagy* **9**, 1367–1385 (2013).
66. S. Patergnani *et al.*, Antipsychotic drugs counteract autophagy and mitophagy in multiple sclerosis. *Proc. Natl. Acad. Sci. U.S.A.* **118**, 2020078118 (2021).
67. M. R. Wieckowski, C. Giorgi, M. Lebedzinska, J. Duszynski, P. Pinton, Isolation of mitochondria-associated membranes and mitochondria from animal tissues and cells. *Nat. Protoc.* **4**, 1582–1590 (2009).
68. G. Morciano *et al.*, Impairment of mitophagy and autophagy accompanies calcific aortic valve stenosis favouring cell death and the severity of disease. *Cardiovasc. Res.* **118**, 2548–2559 (2022).
69. A.-N. A. Agip, J. N. Blaza, J. G. Fedor, J. Hirst, Mammalian respiratory complex I through the lens of cryo-EM. *Annu. Rev. Biophys.* **48**, 165–184 (2019).
70. M. V. Shapovalov, R. L. Dunbrack Jr., A smoothed backbone-dependent rotamer library for proteins derived from adaptive kernel density estimates and regressions. *Structure* **19**, 844–858 (2011).
71. H. R. Bridges *et al.*, Structure of inhibitor-bound mammalian complex I. *Nat. Commun.* **11**, 5261 (2020).
72. I. D. Pogozheva *et al.*, Comparative molecular dynamics simulation studies of realistic eukaryotic, prokaryotic, and archaeal membranes. *J. Chem. Inf. Model.* **62**, 1036–1051 (2022).
73. J. Huang *et al.*, CHARMM36m: An improved force field for folded and intrinsically disordered proteins. *Nat. Methods* **14**, 71–73 (2017).
74. M. Bernetti, G. Bussi, Pressure control using stochastic cell rescaling. *J. Chem. Phys.* **153**, 114107 (2020).
75. G. Bussi, D. Donadio, M. Parrinello, Canonical sampling through velocity rescaling. *J. Chem. Phys.* **126**, 014101 (2007).
76. B. Hess, H. Bekker, H. J. C. Berendsen, J. G. E. M. Fraaije, LINCS: A linear constraint solver for molecular simulations. *J. Comput. Chem.* **18**, 1463–1472 (1997).
77. T. E. Cheatham *et al.*, Molecular dynamics simulations on solvated biomolecular systems: The particle mesh Ewald method leads to stable trajectories of DNA, RNA, and proteins. *J. Am. Chem. Soc.* **117**, 4193–4194 (1995).
78. D. Marino *et al.*, MD and docking studies reveal that the functional switch of CYFIP1 is mediated by a butterfly-like motion. *J. Chem. Theory Comput.* **11**, 3401–3410 (2015).
79. E. F. Pettersen *et al.*, UCSF ChimeraX: Structure visualization for researchers, educators, and developers. *Protein Sci.* **30**, 70–82 (2021).
80. W. Humphrey, A. Dalke, K. Schulten, VMD: Visual molecular dynamics. *J. Mol. Graph.* **14**, 27–28 (1996).
81. N. Perta, E. Trucchi, S. Fuselli, G. Bertorelle, Data from "A fixed mutation in the respiratory complex I impairs mitochondrial bioenergetics in the endangered Apennine brown bear." Zenodo. <https://doi.org/10.5281/zenodo.14003790>. Deposited 14 July 2025.